



Carbon coated Na₇Fe₇(PO₄)₆F₃: A novel intercalation cathode for sodium-ion batteries



Thrinathreddy Ramireddy ^{a,1}, Md Mokhlesur Rahman ^{a,*}, Neeraj Sharma ^b, Alexey M. Glushenkov ^{a,c,1}, Ying Chen ^{a,1}

^a Institute for Frontier Materials, Deakin University, Waurn Ponds, VIC 3216, Australia

^b School of Chemistry, University of New South Wales, Sydney, NSW 2052, Australia

^c Melbourne Centre for Nanofabrication, 151 Wellington Rd, Clayton, VIC 3168, Australia

HIGHLIGHTS

- Na₇Fe₇(PO₄)₆F₃ is prepared via a hydrothermal and a solid state reaction.
- Carbon coating is introduced to improve its electrochemical performance.
- Na₇Fe₇(PO₄)₆F₃/C delivers a reversible capacity of 65 mA h g⁻¹ at 100 mA g⁻¹.
- A possible crystal structure and sodium storage mechanism are discussed.

ARTICLE INFO

Article history:

Received 21 June 2014

Received in revised form

10 August 2014

Accepted 11 August 2014

Available online 20 August 2014

Keywords:

Na₇Fe₇(PO₄)₆F₃/C composite cathode

Amorphous carbon

Hydrothermal synthesis

Solid state reaction

Sodium-ion battery

ABSTRACT

Electrode materials are being developed to realise sodium-ion batteries that can provide energy storage solutions. Here, we develop amorphous carbon coated Na₇Fe₇(PO₄)₆F₃, prepared by combining hydrothermal and solid state reaction methods, as an insertion electrode for sodium-ion batteries applications. Na₇Fe₇(PO₄)₆F₃ particles are surrounded by a thin layer (~1.5–2 nm) of amorphous carbon. The Na₇Fe₇(PO₄)₆F₃/C composite cathode undergoes reversible sodium intercalation/de-intercalation with an average operational potential of ~3.0 V (vs Na⁺/Na). This cathode has a capacity of 65 mA h g⁻¹ at 100 mA g⁻¹ current after 60 cycles and features twice higher capacity than that of an uncoated Na₇Fe₇(PO₄)₆F₃ sample. Therefore, the carbon-coated Na₇Fe₇(PO₄)₆F₃ composite presents feasible sodium intercalation/de-intercalation capacity, offering possibilities for developing a low cost, high performance sodium-ion battery positive electrode.

© 2014 Elsevier B.V. All rights reserved.

1. Introduction

Development of new alternative energy storage systems with low cost, high safety and environmentally friendly electrode materials are critical to meet our rising energy demands and, in particular, to facilitate adoption of renewable energy generation. Large-scale electric energy storage is a key enabler for the use of renewable energy. Recently, sodium-ion (Na-ion) battery has been re-highlighted as a smart technology for this application [1]. The use of Na ions instead of Li ions is an encouraging alternative due to the promise of the low cost associated with the abundance of sodium and enhanced stability of non-aqueous electrolytes in these batteries [2,3]. Therefore, a broad application of sodium-ion (Na-

ion) batteries would bring substantial expansion of the existing energy storage market, especially in the renewable energy storage sector.

However, two major issues limit the practical application of Na-ion based systems. The first issue is that the lower negative redox potential of Na⁺/Na as compared to Li⁺/Li (~2.71 and –3.04 V vs. SHE, standard hydrogen electrode) reduces the operating voltage, leading to generally lower energy densities. The second issue is the larger size of Na⁺ ions as compared to that of the Li⁺ ions (1.02 vs 0.59 Å), i.e., Na-ions are about 55% larger in radius than Li-ions, which causes greater change in the host structure upon insertion or removal and often results in poorer cycle life or even sluggish diffusion [1,4]. Therefore, the search for commercially viable Na-ion batteries demands finding and optimizing new electrode materials.

A wide variety of positive electrode (de-intercalation and intercalation) compounds such as layered oxides (Na_xCoO₂) [5],

* Corresponding author.

E-mail address: m.rahman@deakin.edu.au (M.M. Rahman).

¹ Tel.: +61 352272642; fax: +61 352271103.

phosphates ($\text{Na}[\text{Mn}_{1-x}\text{M}_x]\text{PO}_4$) [3], fluorophosphates (NaVPO_4F) [6], hexacyanoferrates (Prussian blue) ($\text{Na}_4\text{Fe}(\text{CN})_6$) [7], and fluorides (FeF_3) [8] have been synthesized and tested in sodium-ion batteries [9]. Most of the present cathodes are referred to oxides, especially the layered Na_xMO_2 . Although layered oxides generally exhibit higher storage capacity, it is still a tough work to elaborate and enhance the structure and thermal stability of these compounds for their applications, particularly for stationary batteries [9–11]. On the other hand, phosphate polyanion have been identified as potential electroactive materials for sodium metal and Na-ion battery applications, because of the strong inductive effect of the PO_4^{3-} group [12], however, some transition metal phosphates such as MnPO_4 is thermally less stable than FePO_4 [13–15]. Therefore, fluorophosphate materials become more attractive due to the addition of inductive effect of fluorine to the effect of phosphate [16]. The combination of $(\text{PO}_4)^{3-}$ and F^- in the anion sub-lattice is expected to enhance the operating voltage due to the higher ionicity of the M–F bond [16,17]. Their robust and stable frameworks often display better capacity retention than the oxide-based cathodes at the expense of slower kinetics [18]. Recently, a series of sodium fluorophosphates, for example, $\text{Na}_2\text{FePO}_4\text{F}$, NaVPO_4F , $\text{Na}_3\text{V}_2(\text{PO}_4)_2\text{F}_3$, $\text{Na}_3\text{V}_2\text{O}_2(\text{PO}_4)_2\text{F}$, $\text{Na}_3\text{V}_2\text{O}_{2x}(\text{PO}_4)_2\text{F}_{3-2x}$ ($x = 0.8$) and $\text{Na}_{1.5}\text{VOPO}_4\text{F}_{0.5}$, have shown to be promising candidates to be considered [19–21]. Inspired by these works, we focus on fluorophosphate materials, particularly, iron based fluorophosphate due to their good thermal stability and reasonably high operating potential.

Here, we report the synthesis and sodium (de)intercalation chemistry of a novel $\text{Na}_7\text{Fe}_7(\text{PO}_4)_6\text{F}_3$ cathode prepared by combining hydrothermal and solid state reactions. To improve the electrochemical performance, $\text{Na}_7\text{Fe}_7(\text{PO}_4)_6\text{F}_3$ particles were coated with amorphous carbon. The $\text{Na}_7\text{Fe}_7(\text{PO}_4)_6\text{F}_3/\text{C}$ composite electrode exhibits a reversible sodium (de)intercalation capacity of 65 mAh g⁻¹ at 100 mA g⁻¹ current after 60 cycles with an average operational potential of ~3.0 V (vs Na^+/Na). Hence, materials synthesis, a possible crystal structure and the prospects of electrochemical performance of this cathode are discussed in this paper.

2. Experimental

2.1. Synthesis of $\text{Na}_7\text{Fe}_7(\text{PO}_4)_6\text{F}_3$

The $\text{Na}_7\text{Fe}_7(\text{PO}_4)_6\text{F}_3$ powder was synthesised by mixing $\text{FePO}_4 \cdot \text{H}_2\text{O}$ and NaF ($\geq 99\%$ purity, Sigma Aldrich) with a molar ratio of 1:1.1 in acetone via ball milling for 24 h. $\text{FePO}_4 \cdot \text{H}_2\text{O}$ was synthesized by annealing $\text{FePO}_4 \cdot 4\text{H}_2\text{O}$ (Sigma Aldrich) in a tube furnace under the flow of 5% H_2/Ar gas mixture at 100 °C for 3 h. The solid mixture was dispersed homogeneously in 30 ml tetraethylene glycol (TEG) with continuous stirring for 30 min. This homogeneous mixture was transferred into an autoclave and heated at 215 °C and kept for 48 h. After cooling naturally, the precipitated solid was separated from the mixture by washing with acetone and centrifugation, followed by drying at 80 °C overnight under vacuum. The dried materials were divided into two parts. One part was used for composite preparation and other part was calcined at 600 °C for 10 h under argon flow.

2.2. Preparation of $\text{Na}_7\text{Fe}_7(\text{PO}_4)_6\text{F}_3/\text{C}$ composite

Suitable amount of overnight vacuum dried sample (3 g) was dispersed in distilled water and ethanol (1:3 v/v; 20 mL), and sucrose solution (0.5 g sucrose/10 mL distilled water) was added. This solution was dispersed by ultra-sonication for 10 min and then concentrated to a dry state. Finally, the dried powder was calcined

at 600 °C for 10 h under argon flow. Solid powder was washed with deionized water and dried in a vacuum oven at 80 °C overnight.

2.3. Material characterization

Initial X-ray diffraction (XRD, PANalytical X'Pert Pro) data were collected using a $\text{CuK}\alpha$ radiation. Additional high-resolution synchrotron XRD data were collected on the Powder Diffraction beamline (10-BM-1) at the Australian Synchrotron using a wavelength (λ) of 0.72721(2) Å, determined using the NIST 660a LaB_6 standard reference material [22]. Powder samples were packed and sealed in 0.3 mm glass capillaries and data were collected for 6 min at ambient temperature using Debye–Scherrer geometry. Rietveld refinements were carried out using the GSAS software suite with the EXPGUI software interface [23,24]. Transmission electron microscopy (TEM) analysis was performed on a JEOL JEM 2100F instrument operated at 200 kV. To test the electrochemical performance, powder samples were mixed with acetylene carbon black (AB) and a binder, carboxymethyl cellulose (CMC), in a weight ratio of 80: 15: 5 in a solvent (distilled water). The slurry was spread onto Al foil substrates and these coated electrodes were dried in a vacuum oven at 90 °C for 24 h. The electrode was then pressed using a disc with a diameter of 25 mm to enhance the contact between the Al foil and active materials. Subsequently, the electrodes were cut to $1 \times 1 \text{ cm}^2$. The electrochemical half cells were assembled in an Ar-filled glove box (Innovative Technology, USA) using CR 2032 coin cells with Na metal as the counter electrode, 1 M NaClO_4 dissolved in propylene carbonate (PC) with 2% FEC (fluoroethylene carbonate) additive as the electrolyte, and Whatman glass microfibre filter (Grade GF/F) as a separator. The cells were galvanostatically charged/discharged in the range of 4.5–2 V with a Land battery testing system. Cyclic voltammetry (CV) tests were performed on a Solartron Analytical electrochemical work station. For the *ex situ* XRD measurements, the cycled electrochemical cells were disassembled in an Ar-filled glove box. The cycled electrodes were taken out and washed with propylene carbonate (PC) to remove the residual electrolyte before data collection.

3. Results and discussion

XRD data were collected to study the crystal structure and phase purity of pristine $\text{Na}_7\text{Fe}_7(\text{PO}_4)_6\text{F}_3$ and $\text{Na}_7\text{Fe}_7(\text{PO}_4)_6\text{F}_3/\text{C}$ composite (Fig. 1(a)). The profiles of the diffraction peaks could be indexed to the hexagonal phase of $\text{Na}_7\text{Fe}_7(\text{PO}_4)_6\text{F}_3$ [JCPDS no. 01-071-5045, space group $P\bar{6}3$ (no. 173)]. In the pattern of the $\text{Na}_7\text{Fe}_7(\text{PO}_4)_6\text{F}_3/\text{C}$ composite, only peaks of hexagonal $\text{Na}_7\text{Fe}_7(\text{PO}_4)_6\text{F}_3$ can be observed, providing the first evidence that the carbon in the composite is amorphous. Fig. 1(b) shows a Rietveld refined fit of the $\text{Na}_{7+x}\text{Fe}_{7-x}(\text{PO}_4)_6\text{F}_3$ model to the synchrotron XRD data with the inset showing an enlarged $15^\circ \leq 2\theta \leq 19.5^\circ$ region. The refined crystallographic parameters for $\text{Na}_{7+x}\text{Fe}_{7-x}(\text{PO}_4)_6\text{F}_3$ were $a = 13.46798(20)$ Å and $c = 6.67482(11)$ Å with $x = 0.51(6)$ or $\text{Na}_{7.51(6)}\text{Fe}_{6.49(6)}(\text{PO}_4)_6\text{F}_3$, and $R_p = 5.26\%$, $wR_p = 8.57\%$, and $\chi^2 = 4.34$. Refined structural parameters are summarized in Table 1. Fig. 1(c) shows an illustration of the crystal structure of $\text{Na}_{7+x}\text{Fe}_{7-x}(\text{PO}_4)_6\text{F}_3$. It should be noted that impurities are present in the $\text{Na}_7\text{Fe}_7(\text{PO}_4)_6\text{F}_3$ sample that are clear in the synchrotron XRD data but difficult to distinguish in the laboratory XRD data. In any case, these impurities decrease in the carbon coated sample and have not been conclusively identified. They are approximated to be on the order of 5–10%.

In terms of the structural model, atomic positions were freely refined leading to chemically reasonable bonding arrangements which are evidenced in the bond valence sums (BVS), shown for the cations in Table 1 [25]. It is interesting to note that there are four

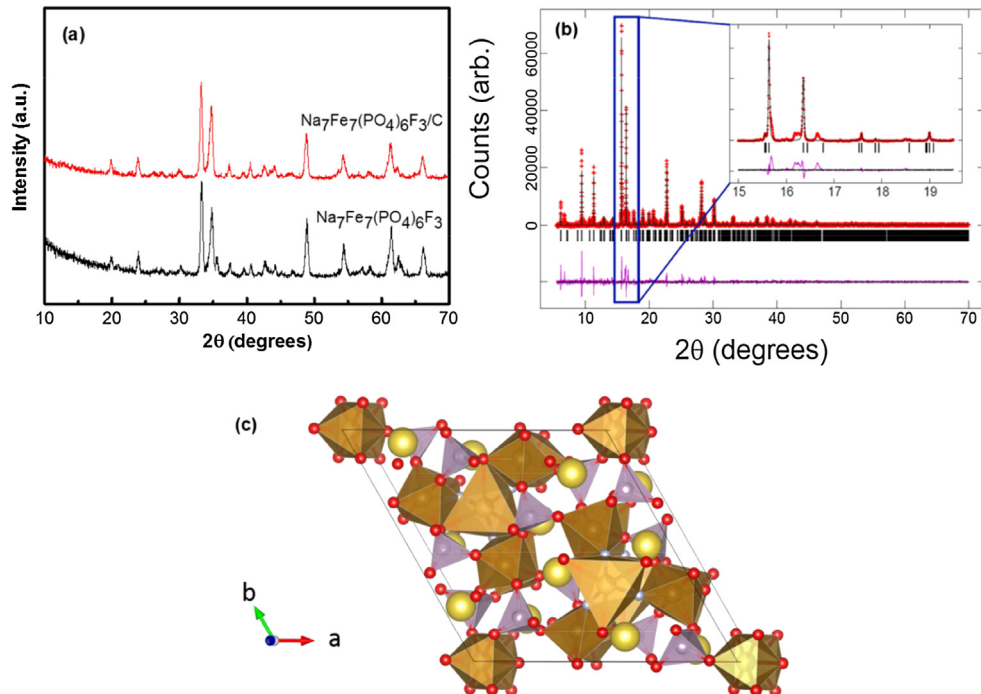


Fig. 1. (a) XRD patterns of Na₇Fe₇(PO₄)₆F₃ and Na₇Fe₇(PO₄)₆F₃/C composite; (b) rietveld refined fit of the Na_{7.26(6)}Fe_{6.75(6)}(PO₄)₆F₃ model to the synchrotron XRD data with the inset showing an enlarged 15 \leq 2θ \leq 19.5 $^{\circ}$ region. Data are shown as crosses, the calculated Rietveld model as a line through the data, and the difference between the data and the model as the line below the data. The vertical reflection markers are for Na_{7.26(6)}Fe_{6.75(6)}(PO₄)₆F₃; and (c) the crystal structure of Na_{7.26(6)}Fe_{6.75(6)}(PO₄)₆F₃ with PO₄ shown in purple and Fe-containing octahedral units in light brown. Oxygen is red, fluorine is light blue and sodium is yellow with the shading indicating occupancy. The central ions in the polyhedra are shown to indicate the orientation, displacements and occupancy. (For interpretation of the references to colour in this figure legend, the reader is referred to the web version of this article.)

possible sites for Na, Fe or mixed Na/Fe occupancy. The Fe (3) and Fe (4) sites were modelled with mixed occupancy due to the smaller observed BVS values ~1, the expected oxidation state of Na, relative to 2 which is the expected oxidation state of Fe. The Na (3) site shows a BVS of ~2 which indicates over-bonding or the presence of Fe on this site. A small amount of Fe on this site would bring the ratio of Na:Fe closer to 1:1, expected from the formula. Unfortunately significant correlation with occupancies and atomic displacement parameters were present for this site which could not be de-convoluted sufficiently to warrant a reasonable understanding of the composition of the site. A similar correlation was observed for the mixed Fe(4)/Na(2) site where a model was generated with freely refining the atomic displacement parameters followed by fixing these and refining occupancies and repeating this procedure until convergence. The result was a significantly larger atomic displacement parameter on the mixed Fe(4)/Na(2) site leading to a higher Fe concentration and a value of x of 0.25(6) in the formula. In order to avoid over-parameterising the model, the atomic displacement parameters were fixed to values found in Table 1. In any case, the structural model presents a good indication of the major phase present in the sample and its lattice and atomic parameters. However, there are four possible crystallographic sites from which Na can be extracted during charge and whether all the sodium-ions can be extracted to provide the theoretical capacity of approximately 160 mAh g⁻¹. The sequence of sodium extraction, e.g. via a solid solution process or any phase transformations, can be determined using *in situ* diffraction based methods which will be the focus of our future work.

Comparing the structural models of the carbon coated and pristine Na₇Fe₇(PO₄)₆F₃ the refined sodium contents (and Na:Fe ratio) are within error of each other suggesting a similar composition in both cases. The major difference appears to be the slight

changes in the small impurities present in the samples. Fig. 2(a) and (b) compare a selected region and illustrate that certain reflections from the impurities increase with others completely disappear, indicated by arrows. Therefore, it appears that the carbon coating significantly influences the impurity distribution or phase composition. Thus the resulting electrochemical performance of the electrode should be interpreted with sufficient consideration of the impurity distribution, as these can act, for example to enhance conduction between particles [26]. Particle size broadening from the Rietveld analysis of the synchrotron XRD data (Figs. 1–2) with the Scherrer equation indicates the pristine Na₇Fe₇(PO₄)₆F₃ is ~175 nm while the Na₇Fe₇(PO₄)₆F₃/C composite is ~100 nm.

Fig. 3 shows the results of SEM and TEM characterisation of pristine Na₇Fe₇(PO₄)₆F₃ and Na₇Fe₇(PO₄)₆F₃/C composite. A typical low magnification SEM images of pristine Na₇Fe₇(PO₄)₆F₃ (Fig. 3(a)) and Na₇Fe₇(PO₄)₆F₃/C composite (Fig. 3(b)) show that both samples consist of numerous clusters. However, carbon coated sample reveals smaller clusters than that of the pristine sample. The carbon coating process used sucrose solution as the carbon source, which has the positive effect in preventing the excessive growth of particles to be relatively smaller. TEM bright-field imaging of the pristine Na₇Fe₇(PO₄)₆F₃ sample exhibits a dense agglomerate cluster (Fig. 3(c)). The high resolution TEM (HRTEM) image (Fig. 3(d)) shows lattice plane contrast consistent with (120) Na₇Fe₇(PO₄)₆F₃ ($d_{120} = 0.44$ nm). The particle(s) of Na₇Fe₇(PO₄)₆F₃/C sample is located over a hole in the holey carbon support film and is surrounded by a thin layer (~1.5–2 nm) of amorphous carbon, marked in Fig. 3(e). The lattice plane is consistent with a single Na₇Fe₇(PO₄)₆F₃ crystal with orientation close to (120).

The electrochemical behaviour of pristine Na₇Fe₇(PO₄)₆F₃ and Na₇Fe₇(PO₄)₆F₃/C composite electrodes were examined noting that the differences in performance are likely to arise from the subtle

Table 1Summary of the structural parameters of $\text{Na}_{7.26(6)}\text{Fe}_{6.75(6)}(\text{PO}_4)_6\text{F}_3$ and selected bond valence sums.

Atom	<i>x</i>	<i>y</i>	<i>z</i>	Site occupancy factor	Isotropic atomic displacement parameter ($\times 100$)/ \AA^2	Bond Valence Sum
Fe(1)	0.2957(11)	0.4268(9)	0.02869	1	1.0 ^b	1.71
Fe(2)	0.2929(11)	0.4178(8)	0.5447(17)	1	1.0 ^b	1.83
Fe(3)	0	0	0.055(4)	0.45(4) ^a	1.5 ^b	1.23
Na(1)	0	0	0.056(4)	0.55(4) ^a	1.5 ^b	1.40
Fe(4)	0.6667	0.3333	-0.035(5)	0.04(4) ^a	1.5 ^b	1.28
Na(2)	0.6667	0.3333	-0.035(5)	0.96(4) ^a	1.5 ^b	1.59
Na(3)	0.2362(21)	0.1857(18)	0.264(4)	1	2.0 ^b	2.27
Na(4)	0.1087(18)	0.4936(17)	0.284(6)	1	2.0 ^b	1.45
P(1)	0.0672(11)	0.2556(12)	0.302(4)	1	0.79(27)	4.62
P(2)	0.6180(12)	0.1111(11)	0.294(4)	1	0.13(22)	4.50
O(1)	0.1376(32)	0.3065(29)	0.433(5)	1	1.72(25) ^c	
O(2)	0.0038(26)	0.1182(25)	0.295(8)	1	1.96(25) ^c	
O(3)	0.1256(32)	0.5672(35)	0.588(7)	1	1.96(25) ^c	
O(4)	0.1417(26)	0.2795(26)	-0.034(5)	1	1.96(25) ^c	
O(5)	0.3841(27)	0.3736(26)	0.288(8)	1	1.96(25) ^c	
O(6)	0.5690(40)	0.1391(29)	0.477(7)	1	1.96(25) ^c	
O(7)	0.4622(26)	0.2463(21)	0.221(5)	1	1.96(25) ^c	
O(8)	0.3352(21)	0.0225(25)	0.263(7)	1	1.96(25) ^c	
F(1)	0.2905(23)	0.5410(19)	0.252(4)	1	1.96(25) ^c	

^a Site occupancies constrained to equal to 1.^b Fixed.^c Constrained to be equal.

differences in the impurities observed in the $\text{Na}_7\text{Fe}_7(\text{PO}_4)_6\text{F}_3$ and the carbon coating on the particles in the composite. Cycling performance of both electrodes at current densities of 15 mA g^{-1} and 100 mA g^{-1} are shown in Fig. 4(a) and (b), respectively. With a low current density of 15 mA g^{-1} , the reversible capacities were 64 and 71 mAh g^{-1} at the end of the 50th cycle for $\text{Na}_7\text{Fe}_7(\text{PO}_4)_6\text{F}_3$ and

$\text{Na}_7\text{Fe}_7(\text{PO}_4)_6\text{F}_3/\text{C}$ electrodes, respectively. In the case of 100 mA g^{-1} current density, the reversible capacity was only 32 mAh g^{-1} for the pristine $\text{Na}_7\text{Fe}_7(\text{PO}_4)_6\text{F}_3$ electrode after 60 cycles whereas it was as high as 65 mAh g^{-1} for the $\text{Na}_7\text{Fe}_7(\text{PO}_4)_6\text{F}_3/\text{C}$ electrode for the same number of cycles. Therefore, the obtained reversible capacity behaviour was almost the same for the two electrodes at a low current density of 15 mA g^{-1} , while the reversible capacity of the $\text{Na}_7\text{Fe}_7(\text{PO}_4)_6\text{F}_3/\text{C}$ electrode has been significantly improved compared to pristine $\text{Na}_7\text{Fe}_7(\text{PO}_4)_6\text{F}_3$, when the cell was cycled at a higher current rate.

At the low current density of 15 mA g^{-1} , the differences between the reversible capacities of both electrodes are actually quite small ~ 7 mAh g^{-1} or about 10%. This is reasonable because the insertion/extraction of Na^+ ions is sufficiently slow at this relatively low current rate. Thus this work confirms that carbon coated particles (and possibly the change in the impurity distribution) can affect the rate-capability of the $\text{Na}_7\text{Fe}_7(\text{PO}_4)_6\text{F}_3/\text{C}$ electrode. The sample prepared without the carbon source (sucrose) exhibits unsatisfactory electrochemical performance under the high-rate experimental condition, presumably because of poor electrical conduction [27]. Amorphous carbon in the $\text{Na}_7\text{Fe}_7(\text{PO}_4)_6\text{F}_3/\text{C}$ composite is able to keep the $\text{Na}_7\text{Fe}_7(\text{PO}_4)_6\text{F}_3$ network electrically connected and thus facilitates the charge transport [4,27]. This carbon coating not only maintains the integrity of the electrodes, but also decreases the polarization, thus enhancing the rate capability of the composite electrode.

Fig. 4 presents the corresponding typical charge/discharge potential profiles for different cycles of $\text{Na}_7\text{Fe}_7(\text{PO}_4)_6\text{F}_3$ (Fig. 4(c)) and $\text{Na}_7\text{Fe}_7(\text{PO}_4)_6\text{F}_3/\text{C}$ (Fig. 4(d)) electrodes at 15 mA g^{-1} in the potential range of 4.5 – 2 V (vs. Na^+/Na). On charging the $\text{Na}_7\text{Fe}_7(\text{PO}_4)_6\text{F}_3$ electrode, the potential exhibits a rapid increase from OCP (2.6 V) to 2.9 V , followed by a gradual increase to 4.0 V and then a steep increase to 4.5 V , as a plateau-like feature is observed in the first charge curve between 2.9 and 4.0 V . Interestingly, the profiles are somewhat different between the first and subsequent charge curves. This may be due to subtle structural re-arrangement during the first charge/discharge or from the impurity phases in the sample. In the subsequent charge cycles, the cell potential drops to 2.1 V (compared with an OCP 2.6 V), followed by a gradual increase to 3.5 V and then a steep

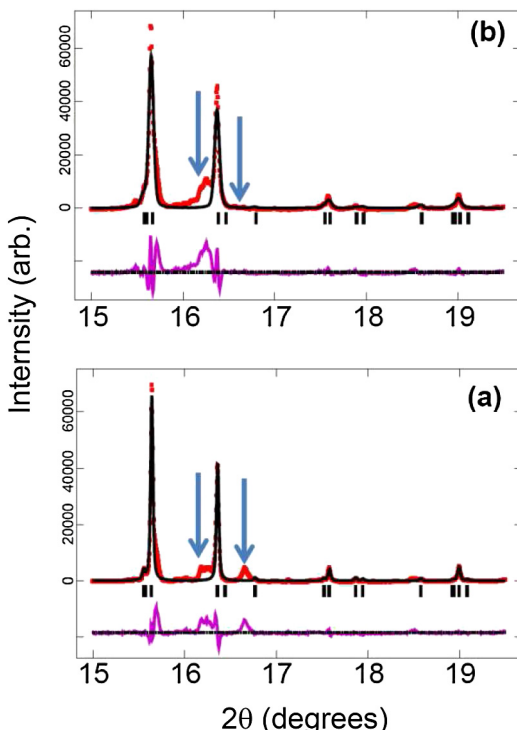


Fig. 2. Rietveld refined fit of the $\text{Na}_7\text{Fe}_7(\text{PO}_4)_6\text{F}_3$ models to the synchrotron XRD data for the (a) pristine and (b) carbon coated samples in the $15 \leq 2\theta \leq 19.5^\circ$ region. Data are shown as crosses, the calculated Rietveld model as a line through the data, and the difference between the data and the model as the line below the data. The vertical reflection markers are for $\text{Na}_7\text{Fe}_7(\text{PO}_4)_6\text{F}_3$. Arrows indicate changes in the impurities present in the sample.

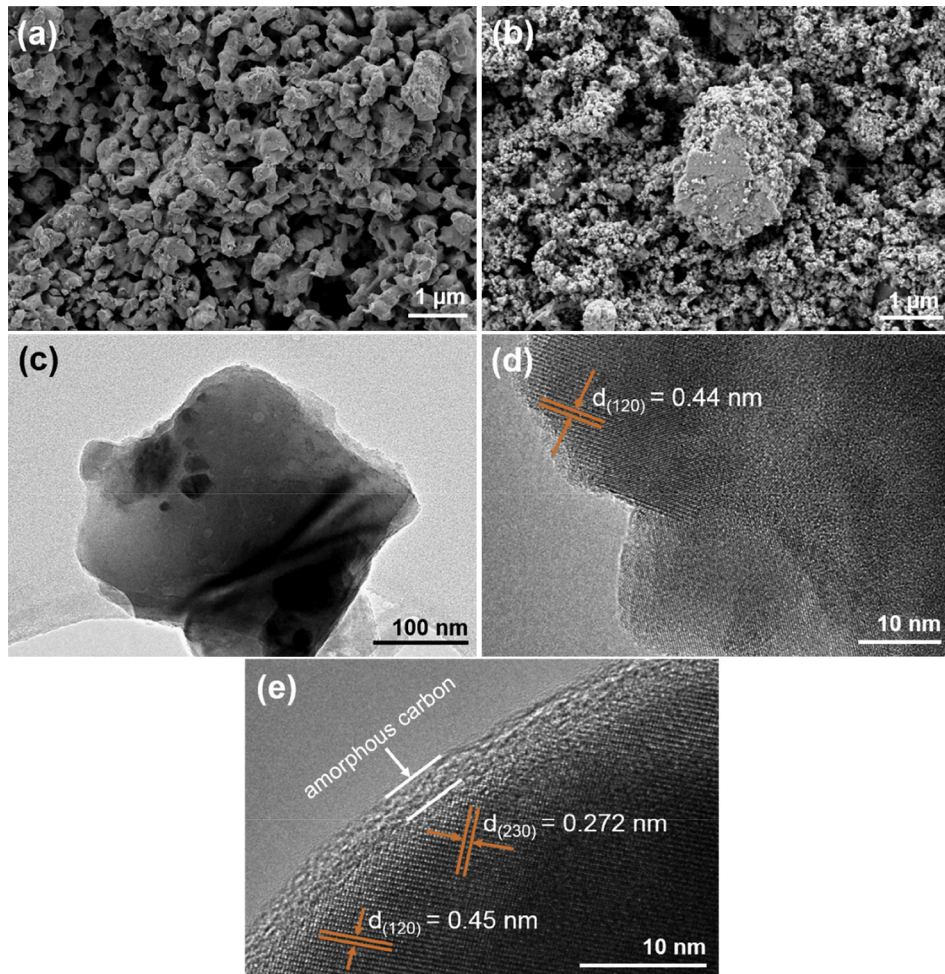


Fig. 3. SEM images (a, b) of (a) $\text{Na}_7\text{Fe}_7(\text{PO}_4)_6\text{F}_3$ and (b) $\text{Na}_7\text{Fe}_7(\text{PO}_4)_6\text{F}_3/\text{C}$ samples. TEM images (c–e) of (c) a bright-field image; (d) the HRTEM image of a $\text{Na}_7\text{Fe}_7(\text{PO}_4)_6\text{F}_3$ crystal; and (e) HRTEM image of a $\text{Na}_7\text{Fe}_7(\text{PO}_4)_6\text{F}_3$ crystal coated with thin layer of amorphous carbon.

increase to 4.5 V. During the first and subsequent discharge cycles, the cell potential drops quickly to 3.25 V, followed by a slow decrease to the cut-off potential of 2.0 V, with a plateau-like feature in the 2.5–2.9 V region. Significant differences are observed in the first charge curves between $\text{Na}_7\text{Fe}_7(\text{PO}_4)_6\text{F}_3$ and $\text{Na}_7\text{Fe}_7(\text{PO}_4)_6\text{F}_3/\text{C}$ electrodes. On charging the cell with the $\text{Na}_7\text{Fe}_7(\text{PO}_4)_6\text{F}_3/\text{C}$ electrode, the cell potential in the first charge gradually increases from OCP (2.3 V) to 3.5 V, followed by a steep increase to 4.5 V. In the subsequent charge cycles, no obvious drop in potential (compared to OCP) is observed and each charge cycle follows essentially the same trend. This may be due to the carbon coating of $\text{Na}_7\text{Fe}_7(\text{PO}_4)_6\text{F}_3$ electrode, where amorphous carbon helps to maintain constant potential in the system during repeated cycling. In the first and subsequent discharge cycles, the cell potential drops quickly to 3.25 V, followed by a slow decrease to the cut-off potential of 2.0 V.

To further assess the electrochemical reactivity of pristine $\text{Na}_7\text{Fe}_7(\text{PO}_4)_6\text{F}_3$ and $\text{Na}_7\text{Fe}_7(\text{PO}_4)_6\text{F}_3/\text{C}$ composite with Na, cyclic voltammetry studies were performed at a scan rate of 0.05 mV s^{-1} in the potential range of 4.5–2 V (Fig. 5). The potential plateaus observed in the charge–discharge curves are consistent with the CV results. Anodic peaks for both electrodes are located at around 3.0 V corresponding to the potential plateau-like feature of the charge process, in which Na^+ ions are de-intercalated from $\text{Na}_7\text{Fe}_7(\text{PO}_4)_6\text{F}_3$ to form $\text{Na}_{7-x}\text{Fe}_7(\text{PO}_4)_6\text{F}_3$. On the other hand,

cathodic peaks are located at around 2.74 V corresponding to the potential plateau-like feature of the discharge process, in which Na^+ ions are intercalated into the $\text{Na}_{7-x}\text{Fe}_7(\text{PO}_4)_6\text{F}_3$ to form $\text{Na}_7\text{Fe}_7(\text{PO}_4)_6\text{F}_3$.

In order to initially understand the Na-storage mechanism in $\text{Na}_7\text{Fe}_7(\text{PO}_4)_6\text{F}_3$, *ex situ* XRD measurements were performed on electrodes before and after cycling (Fig. 6). Fig. 6(a) shows an *ex situ* XRD pattern of the fresh electrode. On first charge to 4.5 V and subsequent discharge to 2.0 V, the XRD patterns still index to the hexagonal phase of $\text{Na}_7\text{Fe}_7(\text{PO}_4)_6\text{F}_3$ (Fig. 6b and c, respectively). However, peak shifts to higher 2θ -values (smaller unit cell volumes) are observed when electrode is charged to 4.5 V due to the release of Na^+ ions from $\text{Na}_7\text{Fe}_7(\text{PO}_4)_6\text{F}_3$. On discharging, the original 2θ -values are effectively retrieved. In terms of unit cell volume, based on highly constrained Rietveld analysis, the original electrode is $1089.1(9)$, at the charged state $1061.0(6)$, and at the discharged state $1094.8(5) \text{ \AA}^3$. This converts to only a 2.6 (2) % decrease in volume during charge. Notably, no peaks of other phases of sufficient intensity were detected in these *ex situ* experiments suggesting an insertion/de-insertion type mechanism during charge/discharge. Unfortunately, these *ex situ* data represent only snapshots of the structure. The true reaction mechanism cannot be determined from such snapshots. In order to avoid speculation we keep the discussion brief and state that further experiments are required.

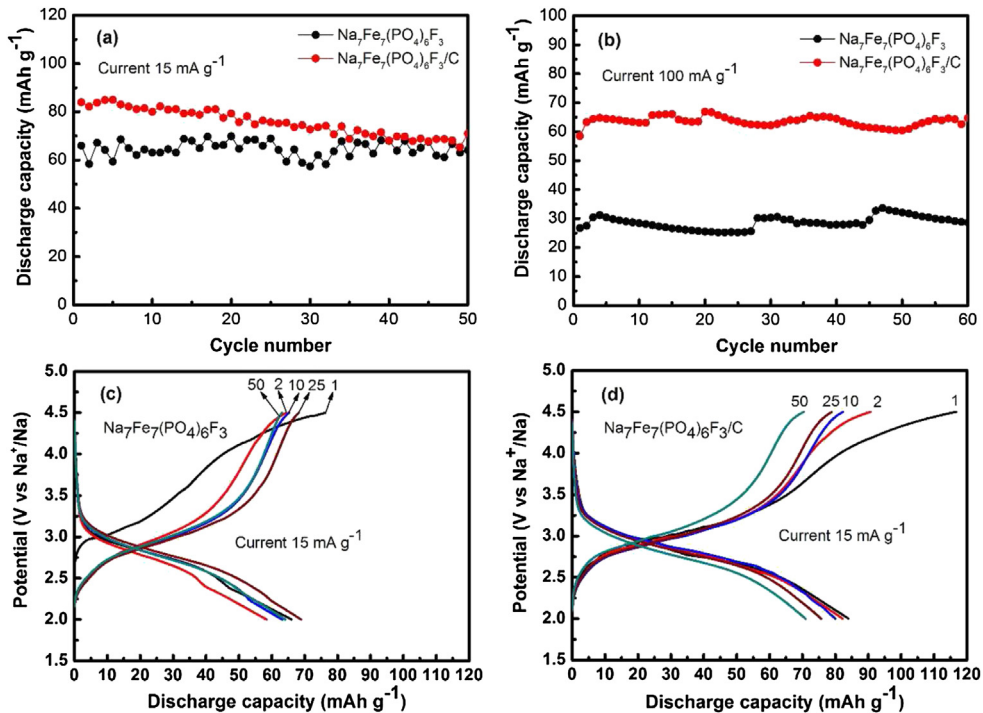


Fig. 4. Electrochemical behaviour of pristine $\text{Na}_7\text{Fe}_7(\text{PO}_4)_6\text{F}_3$ and $\text{Na}_7\text{Fe}_7(\text{PO}_4)_6\text{F}_3/\text{C}$ composite in sodium half cells: (a, b) cycling stability at a low and high current density of 15 mA g^{-1} and 100 mA g^{-1} ; and (c, d) corresponding charge–discharge voltage profiles at a current density of 15 mA g^{-1} .

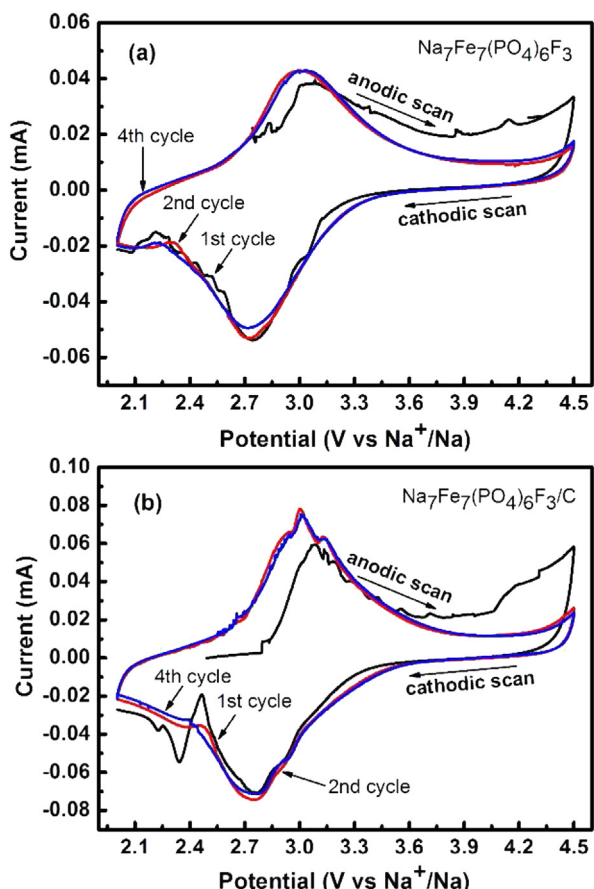


Fig. 5. Cyclic voltammogram of (a) pristine and (b) carbon coated $\text{Na}_7\text{Fe}_7(\text{PO}_4)_6\text{F}_3$ recorded at a scan rate of 0.05 mV s^{-1} in the potential range of $4.5\text{--}2 \text{ V}$.

4. Conclusions

Sodium fluorinated iron phosphate novel cathode, $\text{Na}_7\text{Fe}_7(-\text{PO}_4)_6\text{F}_3$, has successfully been synthesized and the electrochemical de-sodiation/sodiation of $\text{Na}_7\text{Fe}_7(\text{PO}_4)_6\text{F}_3$ was found to be reversible over an extended potential range of $4.5\text{--}2.0 \text{ V}$ vs Na^+/Na . Upon cycling in the potential window of $4.5\text{--}2.0 \text{ V}$, $\text{Na}_7\text{Fe}_7(\text{PO}_4)_6\text{F}_3$ undergoes de-intercalation/intercalation reaction. However, pristine $\text{Na}_7\text{Fe}_7(\text{PO}_4)_6\text{F}_3$ exhibits unsatisfactory electrochemical performance under the high-rate experimental condition, presumably because of poor electrical conduction. Therefore, $\text{Na}_7\text{Fe}_7(\text{PO}_4)_6\text{F}_3$ particles were carbon coated to form $\text{Na}_7\text{Fe}_7(\text{PO}_4)_6\text{F}_3/\text{C}$ composite. The electrochemical performance of the $\text{Na}_7\text{Fe}_7(\text{PO}_4)_6\text{F}_3/\text{C}$ composite was superior to that of the pristine $\text{Na}_7\text{Fe}_7(\text{PO}_4)_6\text{F}_3$ especially at a high current rate. The superior electrochemical performance of

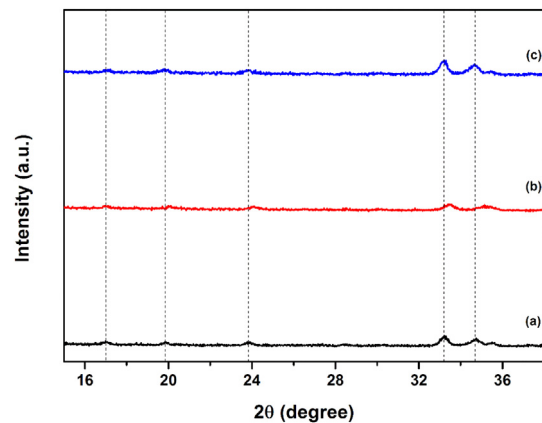


Fig. 6. *Ex situ* XRD patterns of $\text{Na}_7\text{Fe}_7(\text{PO}_4)_6\text{F}_3$ electrodes: (a) fresh electrode (without cycling); (b) first charged state at 4.5 V ; and (c) first discharged state at 2.0 V .

the Na₇Fe₇(PO₄)₆F₃/C composite was attributed mainly to the thin carbon layer which is expected to keep the Na₇Fe₇(PO₄)₆F₃ network electrically connected to facilitate charge transport, maintain the integrity of the electrodes, and decrease polarization, thus enhancing the rate capability of the composite electrode. Using high resolution synchrotron XRD data, impurities were found to differ between the pristine and carbon-coated Na₇Fe₇(PO₄)₆F₃ electrodes which may also contribute to the noted differences in performance at high current rates. Furthermore, this material synthesis strategy can be extended to produce other insertion cathodes for sodium-ion batteries.

Acknowledgements

Financial support from the Australian Research Council under the Discovery Project (DP) Scheme, AINSE Research Fellowship funding for Neeraj Sharma and Deakin University Central Research Grant Scheme, 2014, is acknowledged. Authors also acknowledge the use of electron microscopy facilities in the Victorian Node of the Australian National Fabrication Facility (ANFF).

References

- [1] Y.-U. Park, D.-H. Seo, H.-S. Kwon, B. Kim, J. Kim, H. Kim, I. Kim, H.-I. Yoo, K. Kang, *J. Am. Chem. Soc.* 135 (2013) 13870–13878.
- [2] S. Tepavcevic, H. Xiong, V.R. Stamenkovic, X. Zuo, M. Balasubramanian, V.B. Prakapenka, C.S. Johnson, T. Rajh, *ACS Nano* 6 (2011) 530–538.
- [3] K.T. Lee, T.N. Ramesh, F. Nan, G. Botton, L.F. Nazar, *Chem. Mater.* 23 (2011) 3593–3600.
- [4] A. Langrock, Y. Xu, Y. Liu, S. Ehrman, A. Manivannan, C. Wang, *J. Power Sources* 223 (2013) 62–67.
- [5] C. Delmas, J.-J. Braconnier, C. Fouassier, P. Hagenmuller, *Solid State Ionics* 3–4 (1981) 165–169.
- [6] J. Barker, M.Y. Saidi, J.L. Swoyer, *Electrochem. Solid-State Lett.* 6 (2003) A1–A4.
- [7] J. Qian, M. Zhou, Y. Cao, X. Ai, H. Yang, *Adv. Energy Mater.* 2 (2012) 410–414.
- [8] M. Nishijima, I.D. Gocheva, S. Okada, T. Doi, J.-i. Yamaki, T. Nishida, *J. Power Sources* 10 (2009) 558–562.
- [9] H. Pan, Y.-S. Hu, L. Chen, *Energy Environ. Sci.* 6 (2013) 2338–2360.
- [10] D.D. MacNeil, J.R. Dahn, *J. Electrochem. Soc.* 149 (2002) A912–A919.
- [11] J.R. Dahn, E.W. Fuller, M. Obrovac, U. Von Sacken, *Solid State Ionics* 69 (1994) 265–270.
- [12] P. Serras, V. Palomares, J. Alonso, N. Sharma, J.M. López del Amo, P. Kubiak, M.L. Fdez-Gubieda, T. Rojo, *Chem. Mater.* 25 (2013) 4917–4925.
- [13] S.-W. Kim, D.-H. Seo, X. Ma, G. Ceder, K. Kang, *Adv. Energy Mater.* 2 (2012) 710–721.
- [14] S.-W. Kim, J. Kim, H. Gwon, K. Kang, *J. Electrochem. Soc.* 156 (2009) A635–A638.
- [15] S.P. Ong, A. Jain, G. Hautier, B. Kang, G. Ceder, *Electrochem. Commun.* 12 (2010) 427–430.
- [16] A. Yamada, S.C. Chung, K. Hinokuma, *J. Electrochem. Soc.* 148 (2001) A224–A229.
- [17] N.R. Khasanova, O.A. Drozhzhin, D.A. Storozhilova, C. Delmas, E.V. Antipov, *Chem. Mater.* 24 (2012) 4271–4273.
- [18] R. Tripathi, S.M. Wood, M.S. Islam, L.F. Nazar, *Energy Environ. Sci.* 6 (2013) 2257–2264.
- [19] V. Palomares, P. Serras, I. Villaluenga, K.B. Hueso, J. Carretero-Gonzalez, T. Rojo, *Energy Environ. Sci.* 5 (2012) 5884–5901.
- [20] N. Sharma, P. Serras, V. Palomares, H.E.A. Brand, J. Alonso, P. Kubiak, M.L. Fdez-Gubieda, T. Rojo, *Chem. Mater.* 26 (2014) 3391–3402.
- [21] P. Serras, V. Palomares, T. Rojo, H.E.A. Brand, N. Sharma, *J. Mater. Chem. A* 2 (2014) 7766–7779.
- [22] K.S. Wallwork, B.J. Kennedy, D. Wang, *AIP Conf. Proc.* (2007) 879–882.
- [23] A.C. Larson, R.B. Von Dreele, Book, 1994, pp. 86–748.
- [24] B. Toby, *J. Appl. Cryst.* 34 (2001) 210–213.
- [25] N.E. Brese, M. O'Keeffe, *Acta Crystallogr. Sect. B* 47 (1991) 192–197.
- [26] G. Du, N. Sharma, V.K. Peterson, J.A. Kimpton, D. Jia, Z. Guo, *Adv. Funct. Mater.* 21 (2011) 3990–3997.
- [27] Y. Kawabe, N. Yabuuchi, M. Kajiyama, N. Fukuhara, T. Inamasu, R. Okuyama, I. Nakai, S. Komaba, *Electrochem. Commun.* 13 (2011) 1225–1228.